International Journal of Hydrogen Energy 90 (2024) 218–229

Contents lists available at ScienceDirect

International Journal of Hydrogen Energy

journal homepage: www.elsevier.com/locate/he

Numerical simulation of detonation propagation and extinction in two-phase gas-droplet ammonia fuel

Ruixuan Zhu [a], Guangze Li [b,*], Felix Leach [a,*], Martin Davy [a]

[a] Department of Engineering Science, University of Oxford, Oxford, OX1 3PJ, UK
[b] Hangzhou International Innovation Institute, Beihang University, Hangzhou, 311115, China

ARTICLE INFO

Keywords:
Two-phase ammonia
Detonation propagation
Detonation extinction
Droplet number density
Droplet diameter
Inter-phase interaction

ABSTRACT

Numerical simulations of detonation propagation and extinction in ammonia droplet-laden premixed ammonia–oxygen gas are performed in a 2-D planar channel. The sustained propagation and ultimate quenching of detonation with perturbations from ammonia droplets are observed under lower and larger values of initial droplet number density ($N_{d,0}$) and diameter (d_0), respectively. The detonation always quenches under $d_0 = 15$ μm. The detonation propagation/extinction behaviour and cell structure are dependent on both d_0 and $N_{d,0}$. The positive correlations between droplet volume fraction, inter-phase mass, momentum, and energy transfers and d_0 are more nonlinear than their counterparts of $N_{d,0}$. The post-Mach stem region experiences higher-intensity detonative combustion and thus droplet evaporative, accelerative, and heating effects than the post-incident wave region. During the detonation extinction process, the detonation wave degenerates into detonative spots which then decouple into shock and reaction fronts; gaseous pressure, heat release rate, and nitric oxide volume fraction peaks decline.

1. Introduction

Zero-carbon energy carriers, as alternatives to fossil fuels, are expected to play a pivotal role towards reaching net zero by 2050. Among the energy carriers, ammonia features advantages of high energy density (22.5 MJ/kg), low storage cost (0.54 $/kg-$H_2$ compared to 14.95 $/kg-$H_2$ of pure hydrogen storage), considerable production and transportation volumes (~180 million tons annually) with existing reliable infrastructure [1]. Technologies for unitising ammonia fuel, *e.g.*, in internal combustion engines [2,3] and gas turbines [4,5], have attracted worldwide research interest in recent years. In these research studies, other fuels are commonly added as combustion promoters. This technique tackles the slow chemical kinetics, the consequent slow burning velocity, high ignition energy, narrow flammability range, and poor flame stabilisation of pure ammonia. Other analogous techniques, *e.g.*, pre-chamber turbulent jet ignition [6] and multiple spark plugs [7], have been applied to run conventional engines with pure ammonia. However, the engine operating range typically remains narrow due to the unfavourable characteristics of ammonia for combustion [8]. Detonation offers an inherently higher heat release rate and thermodynamic efficiency than traditional isobaric combustion, which may compensate for poor ammonia combustion properties [9,10]. Therefore, this efficient combustion mode shows huge potential in applying ammonia to propulsion and power generation. Some fundamental experimental studies on ammonia detonation act as premises for its practical applications. Akbar et al. [11] experimentally measured the detonation cell width in ammonia–oxygen (NH_3-O_2) and ammonia-nitrous oxide (NH_3-N_2O) mixtures with and without the dilution effects of nitrogen (N_2) or argon (Ar). The operating conditions cover the Equivalence Ratio (ER) of ϕ = 0.56–1, the initial pressure of p_0 = 55–91 kPa, and the "inert species" mole fraction of $X_{N_2/Ar}$ = 0–0.533. The initial temperature, T_0, is 293 K. Weng et al. [12] later supplemented the detonation velocity and cell width in NH_3-O_2 and NH_3-N_2O mixtures with ϕ = 0.5–1.5, p_0 = 43–100 kPa and ϕ = 0.3–1.25, p_0 = 41–80 kPa, respectively. They also compared the experimental data to analytical solutions, *i.e.*, the Chapman–Jouguet (CJ) detonation velocity and Ng's semi-empirical detonation cell width [13], calculated by Shock & Detonation Toolbox (abbreviated as "SDToolbox" hereafter) [14] and analysed the real gas effect on ammonia detonation. Experiments on flame acceleration and Deflagration-to-Detonation Transition (DDT) in ammonia blends have also been conducted, *e.g.*, in methane–ammonia–oxygen (CH_4-NH_3-O_2) [15], hydrogen-ammonia-air (H_2-NH_3-air) [16,17], and NH_3-O_2 [18] mixtures.

Numerical work on ammonia detonation, *e.g.*, 2-D flame acceleration and DDT in H_2-NH_3-O_2 mixtures [19], 2-D detonation cellular instability [20], 1-D pulsating detonation [21] and end-gas autoignition and detonation [22] in H_2-NH_3-air mixtures, plays a significant

* Corresponding authors.
E-mail addresses: liguangze@buaa.edu.cn (G. Li), felix.leach@eng.ox.ac.uk (F. Leach).

https://doi.org/10.1016/j.ijhydene.2024.09.432
Received 25 April 2024; Received in revised form 26 September 2024; Accepted 29 September 2024
Available online 4 October 2024

complementary role. The detonative combustion of ammonia blends in these studies is characterised by much higher pressure and temperature than deflagration. Therefore, lower pollutant emissions of nitrogen oxides (NO_x) which considerably decrease from medium pressure to high pressure but slightly increase as temperature rises according to Xiao et al. [23] are expected. Detonation propulsion systems, *e.g.*, Pulse Detonation Engines (PDE) [24] and Rotating Detonation Engines (RDE) [25], fuelled by ammonia may then provide a cleaner way of ammonia utilisation.

The study of ammonia RDE has been recently reported but is still in its infancy. Huang et al. [9,10] first experimentally realised NH_3-(O_2 enriched) air and NH_3-O_2 continuous rotating detonation (CRD) in a hollow chamber with Laval nozzle. The NH_3-(O_2 enriched) air CRD only maintains stable propagation when the oxygen mass fraction is over 43%. In a selected test, it propagates at 1753 m/s which represents 77.16% of the corresponding CJ velocity. The operating range of NH_3-O_2 CRD is large — the lean limit is $\phi = 0.24$ with a nozzle contraction ratio of 2, 4, and 6. NH_3-O_2 CRD propagation velocities account for 70%–100% of the corresponding CJ velocities for all the tests. Sun et al. [26] performed 3-D simulations of a RDE in NH_3-H_2-(O_2 enriched) air mixtures. The detonations propagate stably under a wide range of ϕ only with the minimum hydrogen mole concentration of 0.2 in the fuel. The NO_x emissions show a logarithmic decreasing trend in the range of ϕ = 0.7–1.4. The effects of injection total temperature, *i.e.*, T_i, and NH_3/H_2 ER, *i.e.*, ϕ_{NH_3}/ϕ_{H_2}, under a fixed global ER of $\phi_{NH_3} + \phi_{H_2} = 1$ on the feasibility and performance of NH_3-H_2-air RDE were analysed by Wang et al. [27]. The successful detonation propagation was found to benefit from higher T_i but lower ϕ_{NH_3}. The maximum ϕ_{NH_3} reaches 0.6, achieved at T_i = 1000 K.

The foregoing efforts in developing detonation-based ammonia utilisation have so far focused on ammonia as fuel in the gas phase. As ammonia is normally stored in liquid, practical combustion applications of gaseous ammonia require prior vaporisation of liquid ammonia from storage tanks. For example, a 50 kW class micro gas turbine firing ammonia [28,29] was equipped with a vaporiser. Its fuel supply line from the vaporiser to the combustor was heated to avoid fuel vapour condensation. Thus, the need for supply line heating necessarily prolongs the start-up time in ammonia gas turbines. A 2 MW class ammonia-natural gas co-fired gas turbine [30,31] further used an accumulator for the ammonia gas after vaporisation. The maximum ammonia heat fraction in the fuel by Lower Heating Value (LHV) was only 20%, limited by the capacity and performance of the vaporiser and the accumulator. Large-size vaporisers and accumulators to ensure a stable supply of ammonia with higher fractions may amount to huge costs and space requirements. These drawbacks of gaseous ammonia as fuel can be mitigated by supplying ammonia in the liquid phase and direct burning of the ammonia spray. Some early attempts on stabilising liquid ammonia spray flames, *e.g.*, in gas turbine combustors [32,33] and under engine-relevant ambient conditions [34], were unsuccessful — likely as a result of flash boiling effects and the high latent heat of ammonia vaporisation, the endothermic nature of ammonia deposition, and the slow chemical kinetics of ammonia oxidation [35]. Recently, however, Okafor et al. [36,37] reported successful liquid ammonia spray flames in swirl combustors. They achieved the stable combustion of the liquid ammonia spray with the application of preheated swirling air. They found that the co-combustion of the liquid ammonia spray with methane could further improve the flame stability, mitigate the emission of nitrous oxide (N_2O) but encourage the emission of nitric oxide (NO). Zhang et al. [38] experimentally visualised the ignition and diffusion combustion process of the liquid phase ammonia spray ignited by diesel jet in a constant volume vessel. Some simulations also shed light on the characteristics of liquid ammonia spray flames but these studies in the literature are still scarce [39–41].

The aforementioned studies enlighten the possibility of detonation propulsion systems running on the liquid ammonia spray as fuel. One of the challenges is to achieve stable detonative combustion of the liquid ammonia spray while avoiding detonation extinction. This work provides an understanding of this issue. Detonation propagation and extinction in two-phase gas-droplet ammonia fuel, affected by the initial ammonia droplet number density and diameter, are numerically investigated. In the rest of the paper, the modelling details of the numerical method and physical problem are introduced in Section 2. The numerical results are discussed in Section 3. Detonation propagation/extinction scenarios and two-phase gas-droplet interactions, affected by the initial ammonia droplet number density and diameter, are addressed, followed by a computational visualisation of the droplet-laden detonation physico-chemical structure and an analysis of the detonation extinction process. The conclusions are drawn in Section 4.

2. Modelling details

2.1. Numerical solver and method

The detonation propagation and extinction in two-phase gas-droplet ammonia are modelled by a numerical solver, AHISsprayDetFoam [42,43], within the OpenFOAM 10.0 framework [44]. A detailed chemical mechanism for ammonia combustion including 32 species and 203 reactions [45] is applied. The AHISsprayDetFoam solver is a compressible multi-component reactive two-phase gas-droplet flow solver based on the Eulerian–Lagrangian method. It is customised from the OpenFOAM built-in density-based non-reactive rhoCentralFoam solver [46] and coupled with the following modules. First, the mixture-averaged diffusion model [47] is applied to calculate molecular dynamic viscosity, mass, and thermal diffusivities in multi-component mixtures. It has been proven to show comparable accuracy but is relatively computationally efficient against the most precise and sophisticated multi-component diffusion model in simulations of both turbulent and laminar flames [48,49]. Second, the OpenFOAM built-in Lagrangian solver is incorporated to track the dispersed droplets. Droplets at high Reynolds numbers may occur in detonative combustion in two-phase gas-droplet flows with high gas density and inter-phase velocity difference. The droplet sub-models of drag coefficient and convective heat transfer coefficient are optimised, based on Eq. (10) from Hasadi et al. [50] and Whitaker correlation [51], respectively, to fit in the modelling of such droplets. Last, a sparse stiff chemistry solver based on dynamic adaptive hybrid integration (AHI-S) [52] is implemented to speed up the stiff chemistry integration. It has been proven to eclipse OpenFOAM built-in implicit chemistry solvers in computational efficiency with comparable accuracy in simulations of 0-D autoignition and unsteady Perfectly Stirred Reactors (PSR), and 1-D unstrained flames [52,53].

The Eulerian method treats the gas phase as a continuum. The set of governing equations for the gas phase includes the conservation of mass, momentum, species mass fractions, and energy. They are discretised using the cell-centred Finite Volume Method (FVM). A first-order splitting scheme is used to separate the solutions of chemical and non-chemical terms. The chemical terms exist in the species mass fraction and energy equations. In the first step, they are solved over one time step using the AHI-S chemistry solver [52]. The AHI-S solver combines the dynamic Adaptive Hybrid Integration (AHI) method [54] with a sparse matrix technique [55]. The integration of fast and slow chemistry uses the first-order Euler implicit and explicit schemes for time discretisation, respectively. In the second step, the non-chemical terms are integrated over the time step along with the chemical terms calculated from the first step. The second-order implicit Crank–Nicolson scheme [56] is used for time discretisation. An operator-splitting approach is used to solve the transport terms in the momentum and energy equations. Specifically, an explicit predictor equation for the convection of conserved variables and an implicit corrector equation for the diffusion of primitive variables are solved in sequence. The solutions of convective terms in the mass, momentum, and energy equations

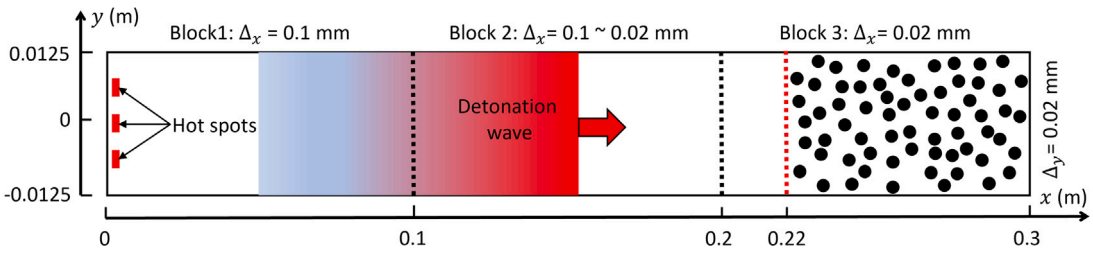

Fig. 1. Schematic of 2-D computational domain filled with premixed NH_3-O_2 gas. Circles: illustrative ammonia droplets.

employ the second-order semi-discrete, non-staggered, and central-upwind Kurganov, Noelle and Petrova (KNP) scheme [57] with a van Leer flux limiter [58]. The convective term in the species mass fraction equation is solved using a Total Variation Diminishing (TVD) scheme to ensure the scalar boundness. The diffusion terms exist in the momentum, species mass fraction, and energy equations. They are split into orthogonal and non-orthogonal parts to minimise the non-orthogonality error. The solutions of the orthogonal and non-orthogonal parts employ the second-order Gauss scheme with linear interpolation and the surface interpolation of variable normal gradients, respectively.

The Lagrangian method considers the liquid phase as dispersed spherical droplets. The droplets are computed with hybrid Lagrangian particle tracking [59] and stochastic parcel [60] method using the Lagrangian solver. The set of governing equations for the liquid phase includes the evolutions of mass, velocity, and temperature for each individual droplet. They are integrated using the first-order Euler implicit scheme for time discretisation. The estimation of droplet evaporation rate in the mass equation follows Ref. [61]. The drag force [62] and Pressure Gradient Force (PGF) are exerted on the droplet in the velocity equation, while other lower-magnitude forces *e.g.*, gravity and Magnus lift force, are neglected. The convective heat transfer rate and evaporation-induced heat transfer rate at the droplet surface are involved in the temperature equation. The interactions among the droplets, *e.g.*, coalescence and collision, are neglected, as only two-phase flows with dilute droplets whose volume fraction is typically less than 0.4% are simulated [63]. The gas and liquid phases are two-way coupled. In this manner, the liquid phase solutions necessitate some gas phase quantities, *e.g.*, temperature, density, velocity, and pressure, at the droplet location and also provide the inter-phase exchange terms of mass, momentum, species, and energy for the gas phase solutions. The inter-phase exchange terms are updated at each time step.

Some analogous numerical solvers coupling rhoCentralFoam with other implicit chemistry solvers and/or the Lagrangian solver (from OpenFOAM standard libraries), *e.g.*, rhoCentralRfFoam [64] and RYrhoCentralFoam [65], are widely used in detonation researches. The rhoCentralRfFoam solver functions well on computing 1-D planar hydrogen-air detonation [64], 2-D methane-air and hydrogen–oxygen–argon detonation [66,67] propagation processes. The RYrhoCentralFoam solver shows accuracy in numerically capturing flow discontinuities from shock and expansion waves, shock-flame interactions, individual droplet evaporation, and two-way gas-droplet coupling in a series of benchmark cases against experimental data and/or analytical solutions [65]. Its capabilities in simulations of rotating detonations [68–71] and detonative combustion in two-phase gas-droplet flows [72–75] have also been confirmed. Accordingly, the AHISsprayDetFoam solver is expected to accurately predict overall characteristics and transient behaviours of the detonation propagation and extinction in two-phase gas-droplet ammonia fuel.

2.2. Physical problem and validation

The target computational configuration in this work is a 2-D planar channel, shown in Fig. 1. Its dimensions are selected following those used by Xu et al. [76,77] in simulations of H_2-air detonation with

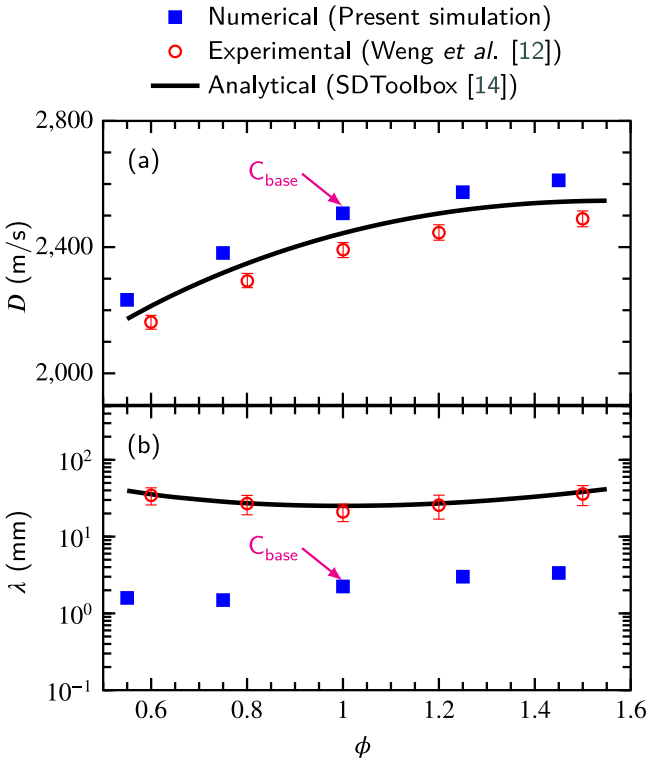

Fig. 2. Numerical, experimental, and analytical results of detonation (a) velocity, D, and (b) cell width, λ, with respect to equivalence ratio, ϕ, in droplet-free premixed NH_3-O_2 gas. C_{base}: the baseline case with $\phi = 1.0$.

perturbations from fine water sprays and dilute inert particles. The coordinate origin lies at the centre of the left end. The length and width along x- and y-directions, *i.e.*, the streamwise and spanwise directions, respectively, are 0.3 and 0.025 m. Following Refs. [76,77], the simulated domain is open to the surroundings at the left and right ends where the "zeroGradient" boundary condition is specified for all variables. The top and bottom ends are assumed to be periodic with the boundary conditions of all variables set as "cyclic". Note that 1-D and 2-D scenarios are still treated as 3-D in OpenFOAM by discretising the reduced directions (z-direction here) with one mesh and enforcing the "empty" boundary condition for all variables. The height of the simulated domain along z-direction, *i.e.*, 0.2 mm, affects some quantities of the liquid phase, *e.g.*, droplet number density, N_d, and volume fraction, V_{fd}, and further affects the gas phase solutions.

The 2-D geometry includes detonation driver (x = 0–0.1 m), development (x = 0.1–0.22 m), and two-phase (x = 0.22–0.3 m) sections. They are filled with premixed NH_3-O_2 gas at $t = 0$. In the gas phase, the initial velocity is zero; the initial temperature, T_0, and pressure, p_0, are 295 K and 71 kPa, respectively; the fuel-oxidiser equivalence ratio, ϕ, ranges from 0.55 to 1.55. The detonation propagation and extinction in the droplet-laden carrier gas are only simulated for the baseline

case with $\phi = 1.0$ in the gas phase. The Detonation Wave (DW) is initiated by three 2 mm-thick Hot Spots (HS) with high pressure ($100p_0$) and high temperature ($10T_0$) vertically placed at the left end of the detonation driver section. This ignition method has been widely used, *e.g.*, in Refs. [65,76,77], as the interactions between the DW from each individual HS quickly trigger detonation frontal instabilities. The DW is a complex of preceding Shock Front (SF) and auto-igniting Reaction Front (RF) with an in-between induction zone. Its frontal instabilities are observed in the form of a series of transient detonation cells whose apexes represent the locations where triple points on the detonation front collide [78], seen later in Section 3.1. Note that preliminary tests with a lower HS pressure ($50p_0$) cannot successfully initiate a DW but with a higher HS pressure ($200p_0$) initiate a highly overdriven DW. The x/y-direction mesh size within the detonation driver section is $\Delta_x = \Delta_y = 0.1$ mm (Block 1).

The DW upon initiation propagates downstream and later enters the detonation development section which is discretised using non-uniform meshes along x-direction transiting from $\Delta_x = 0.1$ mm at $x = 0.1$ m to $\Delta_x = 0.02$ mm at $x = 0.2$ m (Block 2). The y-direction mesh size is $\Delta_y = 0.05$ mm in Block 2. Block 3 starting at $x = 0.2$ m as the main focus sees the minimum and uniform x/y-direction mesh size of $\Delta_x = \Delta_y = 0.02$ mm. The total mesh grid number in Blocks 1, 2, and 3 is 12,500,000. The Half Reaction Length (HRL) of the Zel'dovich–Neumann–Döring (ZND) structure predicted by SDToolbox [14] is $l_{1/2} = 0.83$ mm for the baseline case. The x-direction mesh size of $\Delta_x = 0.02$ mm in Block 3 corresponds to about 42 grids in the HRL and over 42 grids in the thickened induction zone of the DW within the two-phase section due to droplet breakup, heating, and vaporisation [79]. The magnitude of the physical time step, Δt, corresponds to 10^{-10} s for the detonation propagation and extinction in Block 3, with the Courant–Friedrichs–Lewy (CFL) number of the gas phase set as 0.05.

Inside the two-phase section, initially, quiescent and mono-sized ammonia droplets are randomly distributed. Their initial temperature, $T_{d,0}$, density, $\rho_{d,0}$, and heat capacity, $c_{pd,0}$, are 232.9 K, 689.9 kg/m^3, and 4406.6 J/(kg K), respectively. Different combinations of the initial droplet number density, $N_{d,0} = 1.0 \times 10^{12}$, 1.5×10^{12}, or 2.0×10^{12} /m^3, and diameter, $d_0 = 5$, 10, or 15 μm, are considered.

The numerical accuracy of the present simulations in predicting the critical quantities of the two-phase gas-droplet ammonia detonation is premised upon those of the corresponding gaseous ammonia detonation. Therefore, it is conducive to first validate the detonation velocity, D, and cell width, λ, in the droplet-free carrier gas against the experimental measurements by Weng et al. [12] and analytical solutions, *i.e.*, the CJ detonation velocity and the Ng's semi-empirical detonation cell width [13], calculated by SDToolbox [14]. Fig. 2 shows the numerical, experimental, and analytical results of D and λ with respect to ϕ. In Fig. 2(a), the values of D from the present simulations are the averaged propagation speed of the DW from $x = 0.2$ to 0.3 m in Block 3. They are calculated based on the movement of the RF (or the SF) over the corresponding time interval, *e.g.*, 80–119 μs for the baseline case, *i.e.*, C_{base} marked in Figs. 2(a) and (b). The locations of RF and SF are identified where the Heat Release Rate (HRR) and the magnitude of the pressure gradient, $|\nabla p|$, peak, respectively. Other criteria, *e.g.*, the mass fraction of ammonia (Y_{NH_3}), are also tested but yield nearly identical results on the location identification. The numerical results of D see an evolutionary tendency regarding ϕ in agreement with the experimental and analytical data. Their magnitudes show good accuracy and are slightly overestimated by only about 5% and 2.5% against the experimental and analytical data, respectively. Note that the numerical overpredictions of D in comparison with the corresponding CJ detonation velocities suggest slightly overdriven detonations initiated using the ignition method in the present simulations, according to Ref. [78].

In Fig. 2(b), the values of λ from the present simulations are the averages of maximum and minimum cell widths of the DW near $x = 0.3$ m in Block 3. The detonation cells are recorded by the trajectory of peak pressure, p, in each mesh as the DW propagates downstream. The numerical results of λ are less dependent on ϕ than the experimental and analytical data. Their magnitudes are highly underestimated and represent only about 10% of the experimental and analytical data. The noticeable numerical underpredictions of λ are likely associated with the overdriven detonations initiated in the present simulations. For example, the DW reaches the stage of $x/l_{1/2} \approx 360$ at $x = 0.3$ m for the baseline case with $l_{1/2} = 0.83$ mm. The relatively small values of λ are anticipated as a characteristic of the overdriven detonation at this stage, compared to those formed later at the detonation self-sustained propagation stage [80]. Besides, some other influential factors, *e.g.*, unmimicked geometrical configuration and unavoidable nonidealities [81] in the experimental work, and the chemical mechanism, may also play a part in the mismatched experimental/analytical and numerical results of λ. In general, the present simulations respectively fairly overestimate D and underestimate λ of the DW in the premixed NH_3-O_2 gas.

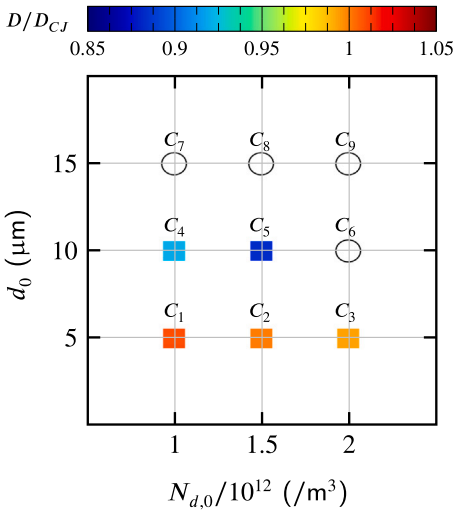

Fig. 3. Diagram of detonation propagation and extinction in droplet-laden premixed NH_3-O_2 gas with different initial droplet number density, $N_{d,0}$, and diameter, d_0. Squares: propagation scenarios; Circles: extinction scenarios.

3. Results and discussion

3.1. Detonation propagation/extinction diagram

The present simulations in the ammonia droplet-laden NH_3-O_2 gas with $\phi = 1.0$ in the gas phase (the baseline case) are parametrised by the initial droplet number density, $N_{d,0}$, and diameter, d_0. The detonation propagation/extinction scenarios with perturbations from the ammonia droplets with $N_{d,0} = 1.0 \times 10^{12}$, 1.5×10^{12}, or 2.0×10^{12} /m^3 and $d_0 = 5$, 10, or 15 μm are summarised in a diagram in Fig. 3. They are labelled as Cases C_1–C_9. The square symbols for Cases C_1–C_5 in the diagram denote the sustained propagation of the DW with the coupled RF and SF until the right end of the two-phase section. They are coloured by the ratio between the averaged propagation speed of the DW over the entire two-phase section and the CJ detonation velocity for the droplet-free baseline case, D/D_{CJ}. The maxima and minima of D/D_{CJ} are 1.01 for Case C_1 with $N_{d,0} = 1.0 \times 10^{12}$ /m^3, $d_0 = 5$ μm and 0.88 for Case C_5 with $N_{d,0} = 1.5 \times 10^{12}$ /m^3, $d_0 = 10$ μm, respectively. The unquenched DWs are attenuated in strength when crossing the ammonia droplets in contrast to their overdriven droplet-free counterpart with $D/D_{CJ} = 1.03$. They are less perturbed under lower values of $N_{d,0}$ and d_0, characterised by lower velocity deficits relative to the corresponding droplet-free detonation velocity. The open

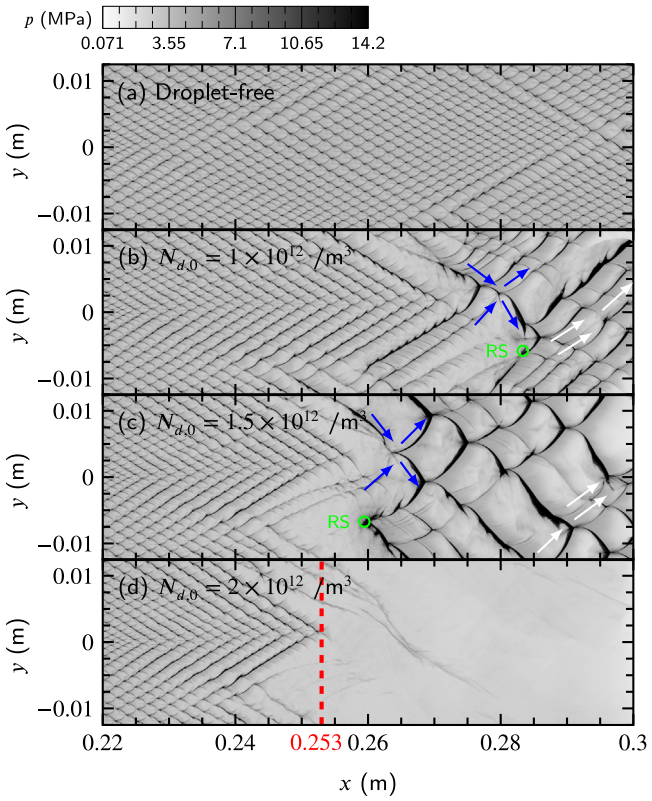

Fig. 4. Trajectories of detonation peak pressure in (a) droplet-free and (b)–(d) droplet-laden premixed NH_3-O_2 gas with initial droplet diameter of $d_0 = 10$ μm. RS: reignition spot. Blue arrows mark triple point collision and thus re-amplification on detonation front; White arrows mark detonation cell merging and splitting.

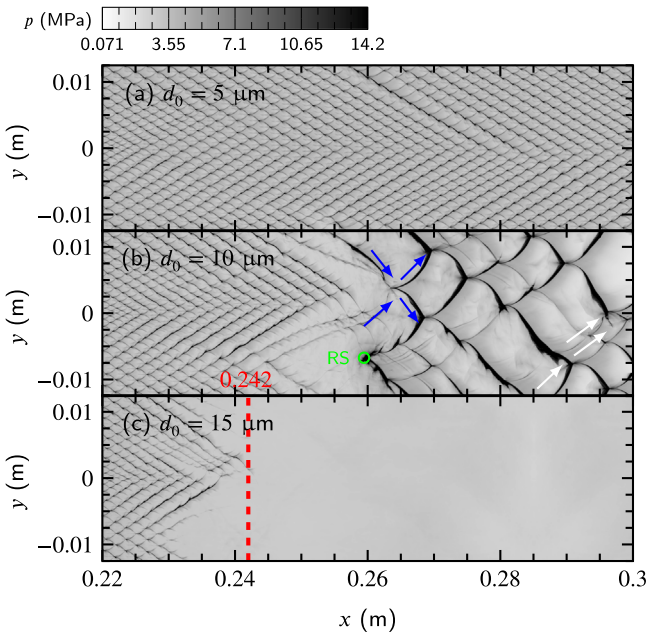

Fig. 5. Trajectories of detonation peak pressure in droplet-laden premixed NH_3-O_2 gas with initial droplet number density of $N_{d,0} = 1.5 \times 10^{12}$ /m^3. RS: reignition spot. Blue arrows mark triple point collision and thus re-amplification on detonation front; White arrows mark detonation cell merging and splitting.

circle symbols for Cases C_6–C_9 in the diagram denote the ultimate quenching of the DW which is characterised by the decoupling of the RF and SF after the DW travels a finite distance within the two-phase section. This situation always occurs under the relatively large initial droplet diameter of $d_0 = 15$ μm for Cases C_7–C_9. Note that the droplet-laden distances that the DWs travel before quenching are shortened as $N_{d,0}$ increases with fixed $d_0 = 15$ μm, though not demonstrated in Fig. 3.

Cases C_4–C_6 with $N_{d,0} = 1.0 \times 10^{12}$, 1.5×10^{12}, and 2.0×10^{12} /m^3, respectively, are selected to further examine the impacts of $N_{d,0}$ on the detonation propagation and extinction under fixed $d_0 = 10$ μm. Fig. 4 depicts the contours of detonation peak pressure trajectories within their two-phase sections and the droplet-free baseline case for comparison. It is seen that the addition of the ammonia droplets in the carrier gas considerably changes the detonation cell structure by different degrees affected by $N_{d,0}$. The propagation/extinction behaviour of the DW is changed accordingly. For the relatively low and intermediate values of $N_{d,0} = 1.0 \times 10^{12}$ and 1.5×10^{12} /m^3 in Figs. 4(b) and (c), the detonation cells partially fade subject to reduced pressure maxima within roughly $x = 0.27$–0.28 m and $x = 0.245$–0.26 m, respectively. It is associated with weakened chemical reactivity at the triple points of the partially decoupled DW. The partial decoupling of the DW with localised thickened induction zones is triggered by the two-phase gas-droplet interactions, elaborated later in Section 3.2. The detonation cells subsequently restore following the temporary fading because of two primary incentives. One is the triple point collision and thus re-amplification on the detonation front; the other is the detonation reignition at a tip of the RF where the shock focusing/collision enhances the localised chemical reactivity [82,83]. The former and the latter are marked by blue arrows and the Reignition Spot (RS), respectively, in Figs. 4(b) and (c). The restored detonation

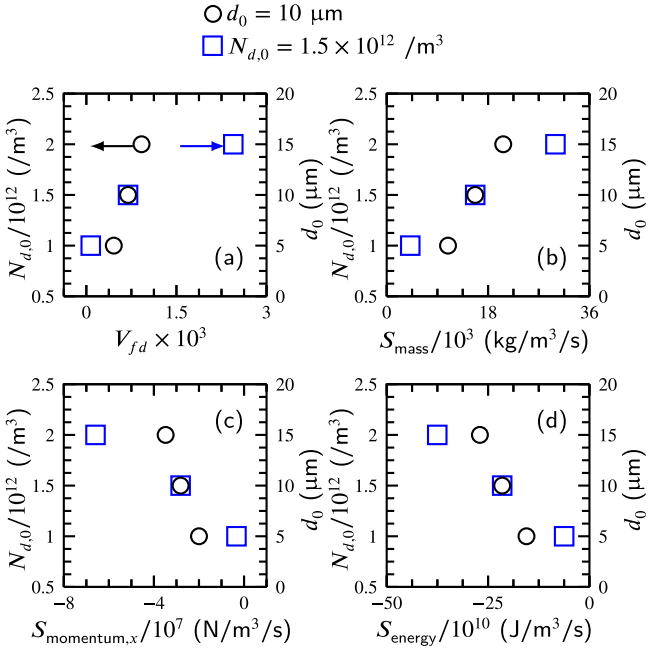

Fig. 6. Time and volume averaged (a) droplet volume fraction, V_{fd}, and inter-phase (b) mass, S_{mass}, (c) momentum along x-direction, $S_{momentum,x}$, and (d) energy exchange rates, $S_{energy,x}$, in droplet-laden NH_3-O_2 gas as functions of initial droplet number density, $N_{d,0}$, (black circle scatters) and diameter, d_0, (blue square scatters) when detonation propagates from $x = 0.22$ to 0.24 m.

cell widths are noticeably increased and positively correlated to $N_{d,0}$. Similar spatial variations of the detonation cells in hydrogen/air gas with fine water sprays were reported by Xu et al. [76]. The detonation frontal instabilities in the post-restoration areas are also enhanced with detonation cell merging and splitting, marked by white arrows in Figs. 4(b) and (c), respectively, observed. For the relatively high value of $N_{d,0} = 2.0 \times 10^{12}$ /m^3 in Fig. 4(d), the detonation cells completely

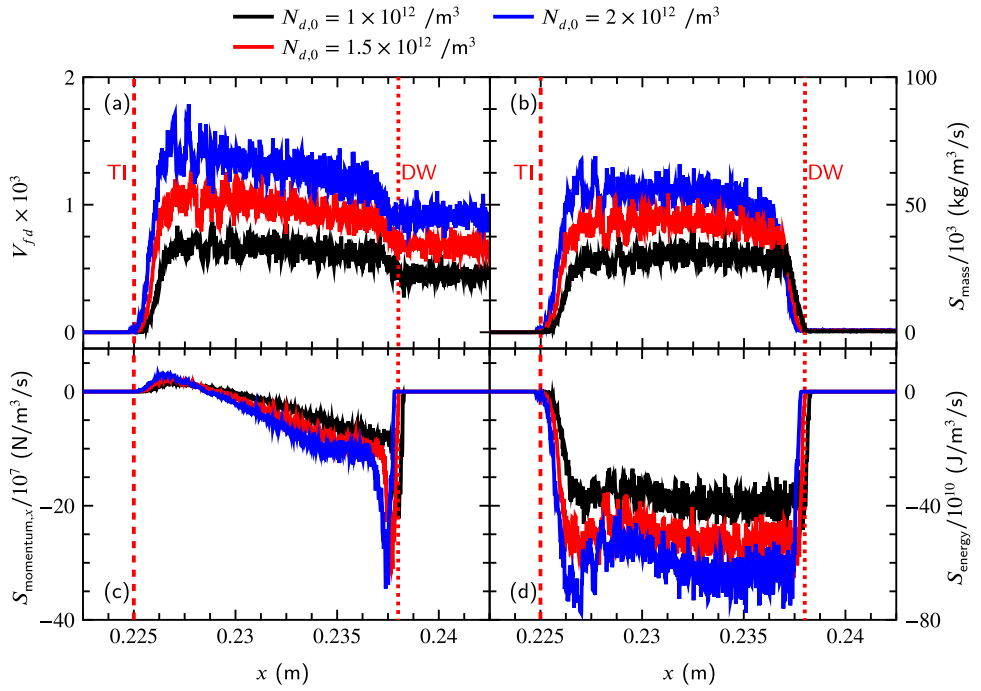

Fig. 7. Spatial profiles of y-direction averages of (a) droplet volume fraction, V_{fd}, and inter-phase (b) mass, (c) x-direction momentum, and (d) energy exchange rates (denoted as S_{mass}, $S_{\text{momentum},x}$, and S_{energy}, respectively) along x-direction in droplet-laden NH_3-O_2 gas with initial droplet diameter of d_0 = 10 μm at 95 μs. DW and TI: the locations of detonation wave and two-phase interface, respectively, for Case C_5 with $N_{d,0} = 1.5 \times 10^{12}$ /m^3.

fade at around x = 0.253 m, *i.e.*, the red dashed line, indicating the quenching of the DW.

Cases C_2, C_5, and C_8 with d_0 = 5, 10, and 15 μm, respectively, are selected to further examine the impacts of d_0 on the detonation propagation and extinction under fixed $N_{d,0} = 1.5 \times 10^{12}$ /m^3. Fig. 5 depicts the contours of detonation peak pressure trajectories within their two-phase sections. Note that Fig. 5(b) with d_0 = 10 μm is the same as Fig. 4(c), where the initial droplet diameter is d_0 = 10 μm . For the relatively low value of d_0 = 5 μm in Fig. 5(a), the DW is almost unperturbed by the ammonia droplets. The detonation cell widths and regularity are mostly sustained. For the relatively high value of d_0 = 15 μm in Fig. 5(c), the DW quenches early at around x = 0.242 m, *i.e.*, the red dashed line, with the complete fading of the detonation cells.

3.2. Two-phase gas-droplet interaction

The numerical results of droplet volume fraction, V_{fd}, two-phase gas-droplet mass, x-direction momentum, and energy exchange rates, *i.e.*, S_{mass}, $S_{\text{momentum},x}$, and S_{energy}, respectively, are firstly analysed in this section. They are compared among the afore-selected representative simulations before the DWs arrive at x = 0.24 m. The critical location of x = 0.24 m is identified slightly ahead where the earliest detonation extinction takes place, *i.e.*, at x = 0.242 m for Case C_8.

The quantitative dependences of V_{fd}, S_{mass}, $S_{\text{momentum},x}$, and S_{energy} on $N_{d,0}$ and d_0 are presented in Fig. 6. The inter-phase exchange quantities are time and volume averaged during the period when the DWs propagate within the two-phase section until x = 0.24 m. The positive values of S_{mass} suggest the mass transfer from the liquid phase to the gas phase, while the negative values of $S_{\text{momentum},x}$, and S_{energy} suggest the momentum and energy transfer from the gas phase to the liquid phase. They match with the evaporation, acceleration, and heating of the ammonia droplets, respectively. When d_0 is fixed at 10 μm, *i.e.*, the black circle scatters, the magnitudes of V_{fd}, S_{mass}, $S_{\text{momentum},x}$, and S_{energy} are found to be positively and approximately linearly correlative to $N_{d,0}$ which varies from 1.0×10^{12}, 1.5×10^{12}, to 2.0×10^{12} /m^3. When $N_{d,0}$ is fixed at 1.5×10^{12} /m^3, *i.e.*, the blue square scatters, whereas, they grow nonlinearly with the increase of d_0 from 5, 10, to 15 μm. The phenomenon is especially significant for V_{fd} as the droplet volume is proportional to the cubic of the droplet diameter. S_{mass}, $S_{\text{momentum},x}$, and S_{energy} occur at the droplet surface which is proportional to the square of the droplet diameter.

Figs. 7 and 8 show the spatial profiles of y-direction averages of V_{fd}, S_{mass}, $S_{\text{momentum},x}$, and S_{energy} along x-direction at 95 μs when the DWs are close to x = 0.24 m. The former includes Cases C_4–C_6 with $N_{d,0} = 1.0 \times 10^{12}$, 1.5×10^{12}, and 2.0×10^{12} /m^3, respectively, under fixed d_0 = 10 μm. The latter includes Cases C_2, C_5, and C_8 with d_0 = 5, 10, and 15 μm, respectively, under fixed $N_{d,0} = 1.5 \times 10^{12}$ /m^3. In addition to the DW, the Two-phase Interface (TI) between the droplet-free and droplet-laden carrier gas is the other characteristic front. The two-phase gas-droplet interactions mainly proceed between the DW and the TI. Consequently, the locations of DW and TI are identified where the magnitudes of S_{mass}, $S_{\text{momentum},x}$, and S_{energy} jump from near-zero and plunge to near-zero, respectively.

In Fig. 7, the locations of the DW and the TI under all the values of $N_{d,0}$ fairly overlap at 95 μs. For example, the DW and the TI lie at around x = 0.238 and 0.225 m, respectively, *i.e.*, the red dotted and dashed lines, for Case C_5 with $N_{d,0} = 1.5 \times 10^{12}$ /m^3. The influences of $N_{d,0}$ on the droplet-laden detonation velocity are not noticeable yet but accumulate onto the detonation propagation/extinction behaviour at later stages, see Figs. 4(b)–(d). The localised fluctuations of V_{fd} in the intact carrier gas ahead of the DW in Fig. 7(a) are attributed to the non-uniformity of droplet number per mesh, as the ammonia droplets are initially randomly distributed. Behind the DW, the droplet motion driven by the flowing carrier gas further strengthens the localised fluctuations of V_{fd}. The values of S_{mass}, $S_{\text{momentum},x}$, and S_{energy} in Figs. 7(b)–(d) also intensely oscillate following V_{fd}. They see climbing magnitudes with the increase of $N_{d,0}$ from 1.0×10^{12}, 1.5×10^{12}, to 2.0×10^{12} /m^3, so does V_{fd}. S_{mass} and S_{energy} are almost constants between the DW and the TI, indicating almost unchanged intensities of the droplet evaporation and heat absorption in the detonated carrier gas. The magnitude of $S_{\text{momentum},x}$ is extremely large closely behind the DW and declines towards the TI. The ammonia droplets which freshly

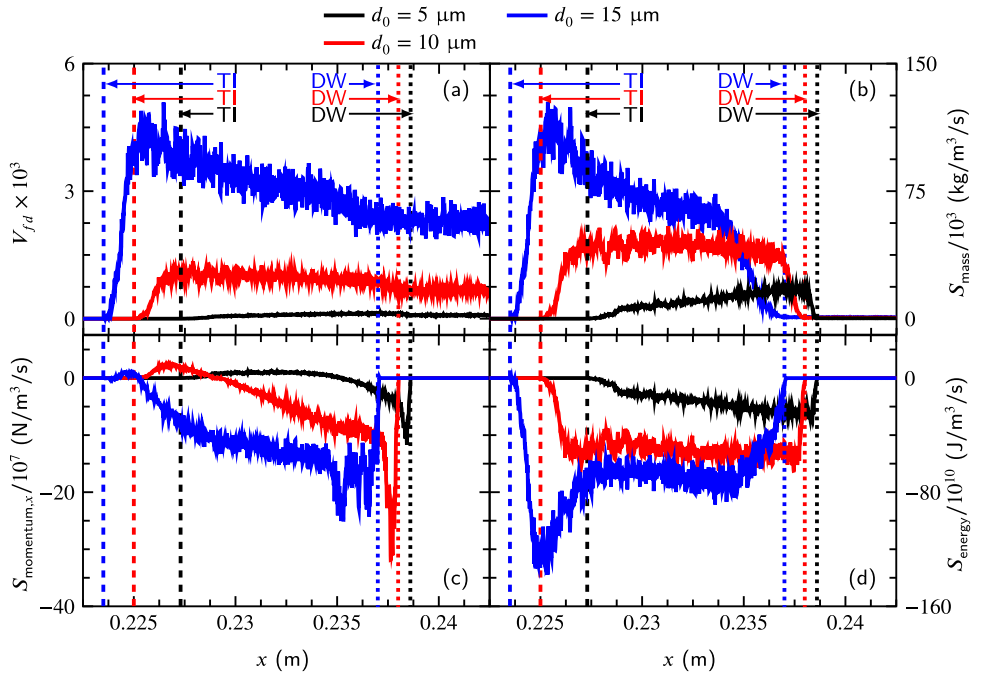

Fig. 8. Spatial profiles of y-direction averages of (a) droplet volume fraction, V_{fd}, and inter-phase (b) mass, (c) x-direction momentum, and (d) energy exchange rates (denoted as S_{mass}, $S_{\text{momentum},x}$, and S_{energy}, respectively) along x-direction in droplet-laden NH_3-O_2 gas with initial droplet number density of $N_{d,0} = 1.5 \times 10^{12}$ /m^3 at 95 μs. DW and TI: the locations of detonation wave and two-phase interface, respectively.

enter the post-DW region respond quickly to the local gaseous velocity. They well follow the local carrier gas and travel ahead rather than pile up ahead of the TI, leading to the nearly uniform V_{fd} between the DW and the TI [84].

In Fig. 8 at 95 μs, the DW and the TI lie at around x = 0.239 and 0.227 m, respectively, *i.e.*, the black dotted and dashed lines, for Case C_2 with d_0 = 5 μm. They lie at around x = 0.237 and 0.224 m, respectively, *i.e.*, the blue dotted and dashed lines, for Case C_8 with d_0 = 15 μm. The locations of the DW and the TI are different among Cases C_2, Case C_5 with d_0 = 10 μm, and C_8. The droplet-laden detonation velocity has been influenced more by the different values of d_0 than $N_{d,0}$ at the particular moment, which supports Fig. 6. The magnitudes of V_{fd}, S_{mass}, $S_{\text{momentum},x}$, and S_{energy} rise on the whole as d_0 grows from 5, 10, to 15 μm. V_{fd}, S_{mass}, and S_{energy} see decreased and increased tendencies in magnitude from the DW to the TI when d_0 = 5 and 15 μm, respectively, in comparison with their almost unchanged values when d_0 = 10 μm. The magnitude of $S_{\text{momentum},x}$ immediately peaks and drops to zero behind the DW when d_0 = 5 μm. It remains non-zero until quite close to the TI with the maxima lasting much longer near the DW when d_0 = 15 μm. These phenomena result from the fact that droplet momentum and thermal response times are positively correlated to the droplet diameter [84]. The ammonia droplets with d_0 = 5 μm are completely evaporated, accelerated, and heated most quickly upon access into the post-DW region. However, those with d_0 = 15 μm are still partially evaporated, comparatively low-speed and thus accumulated ahead of the TI.

The critical quantities of the gas and liquid phases, *i.e.*, gaseous ammonia volume fraction, X_{NH_3}, x-direction velocity, u_x, temperature, T, and droplet diameter, d, x-direction velocity, $u_{d,x}$, temperature, T_d, directly respond to the inter-phase mass, momentum, and energy transfers. Their spatial distributions for Case C_5 with $N_{d,0} = 1.5 \times 10^{12}$ /m^3 and d_0 = 10 μm at 95, 105, and 115 μs are presented in Fig. 9. The three instants correspond to when the detonation cells sustain, fade, and restore, respectively, see Fig. 4(c) or Fig. 5(b). At 95 μs in Fig. 9(a), the DW and the TI are marked in the gaseous and droplet contours, respectively. The detonation frontal instabilities are reflected in the wrinkling of the DW with multiple bumps and depressions. The ammonia droplets right behind the DW and ahead of the TI enter the post-DW region at the earliest and the latest, respectively. The latter whose evaporation, acceleration, and heat absorption are prolonged have relatively small d, high $u_{d,x}$ and T_d compared to the former. The variations of X_{NH_3}, u_x, and T see opposite trends against those of d, $u_{d,x}$, and T_d, respectively, from the DW to the TI. At 105 μs in Fig. 9(b), the DW is partially decoupled and degenerates into the Detonative Spot (DS) at the tip of the RF due to prior perturbations from the ammonia droplets, see the contour of T. Its induction zone is locally thickened subject to RF-SF partial decoupling. At 115 μs in Fig. 9(c), the DW is in a stable propagating state after reinitiation. The droplet-laden detonation front structure consists of the RF and the SF with alternate Mach Stems and Incident Waves connected by the Triple Points, denoted as MS, IW, and TP in the contour of T, respectively, as referred to by Xu et al. [76]. The differences of the gaseous and droplet thermo-chemical states behind the MS and the IW when y = −0.002 and 0.002 m, respectively, are quantitatively described later in Fig. 10.

The distance between the DW and the TI gradually widens from 95, 105, to 115 μs. Meanwhile the differences between the pairs of gaseous and droplet quantities, *i.e.*, X_{NH_3}-d, u_x-$u_{d,x}$, and T-T_d, close to the TI where the inter-phase mass, momentum, and energy transfers are temporally accumulated gradually reduce. Specifically, within the time interval of 95-115 μs, the values of X_{NH_3} and T ahead of the TI increase from 0.013, 0.104, to 0.165 and decline from 2750, 2020, to 1680 K, respectively. The droplet x-direction velocity ahead of the TI is approximately relaxed to the carrier gas x-direction velocity of around 1250 m/s at 115 μs.

Fig. 10 shows the spatial profiles of X_{NH_3}, d, u_x, $u_{d,x}$, T, and T_d along x-direction for Case C_5 with $N_{d,0} = 1.5 \times 10^{12}$ /m^3 and d_0 = 10 μm at 115 μs. The y-direction locations at −0.002 and 0.002 m corresponding to the MS and the IW, respectively, see Fig. 9(c), are selected. In Fig. 10(a), the values of X_{NH_3} slightly fluctuate ahead of the SF as the ammonia droplets slowly evaporate, supported by $d \approx 9.5$ μm, in the intact carrier gas. The gaseous and droplet velocity and temperature fields ahead of the SF are nearly unperturbed. X_{NH_3} plunges to 0.003 across the RF behind both the MS and the IW. The maximum values of u_x occur right behind the MS and the IW with about 1630 and

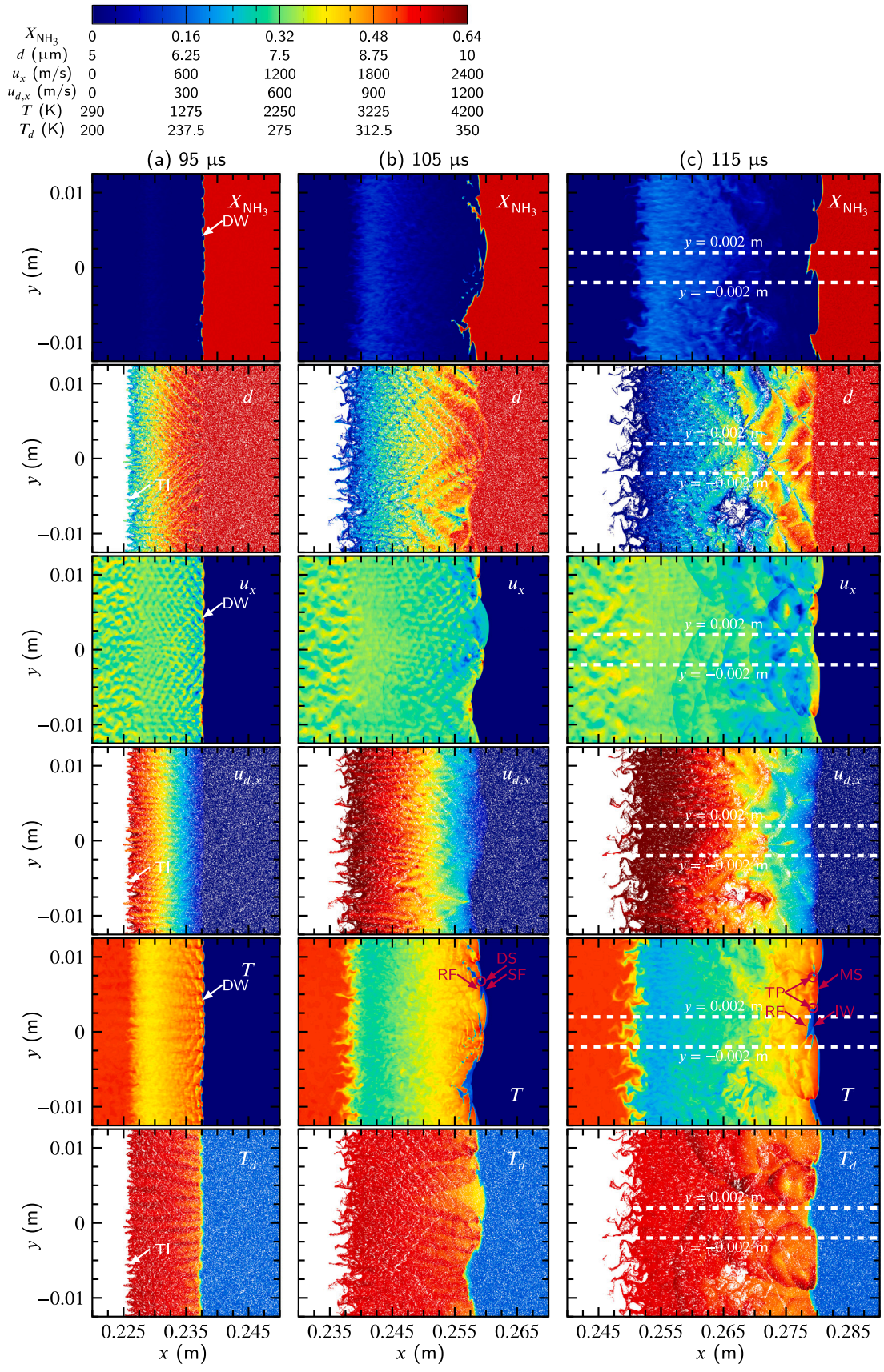

Fig. 9. Spatial distributions of gaseous ammonia volume fraction, X_{NH_3}, droplet diameter, d, gaseous x-direction velocity, u_x, droplet x-direction velocity, $u_{d,x}$, gaseous temperature, T, and droplet temperature, T_d, in droplet-laden NH_3-O_2 gas with initial droplet density number and diameter of $N_{d,0} = 1.5 \times 10^{12}$ /m^3 and $d_0 = 10$ μm at (a) 95, (b) 105, and (c) 115 μs. DW: detonation wave; TI: two-phase interface; RF: reaction front; SF: shock front; DS: detonative spot; MS: Mach stem; IW: incident wave; TP: triple point.

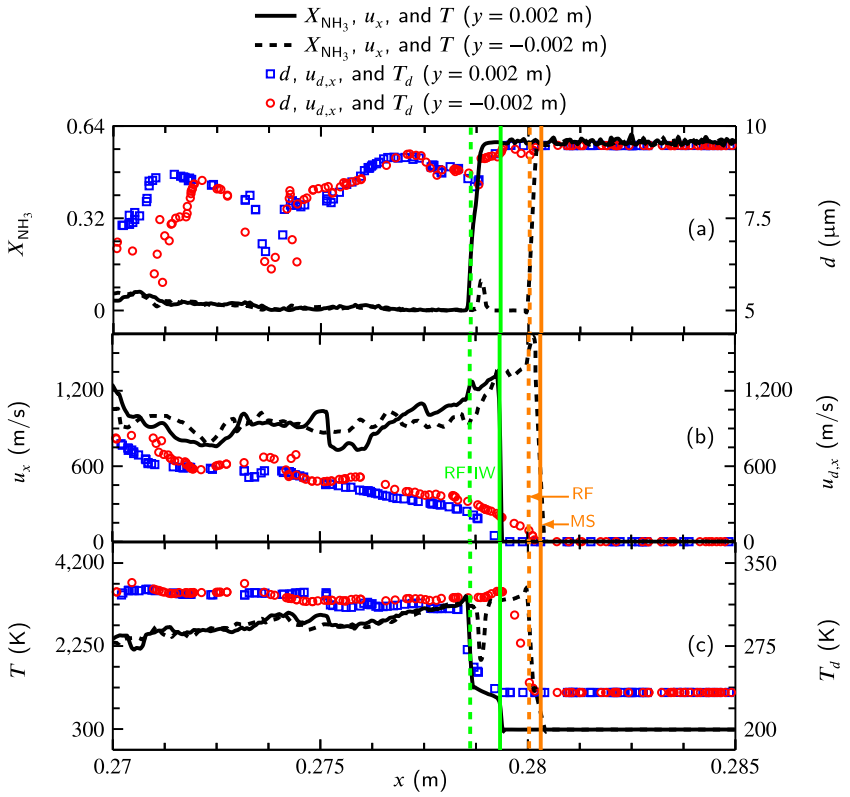

Fig. 10. Spatial profiles of (a) gaseous ammonia volume fraction, X_{NH_3}, and droplet diameter, d, (b) gaseous x-direction velocity, u_x, and droplet x-direction velocity, $u_{d,x}$, and (c) gaseous temperature, T, and droplet temperature, T_d, along x-direction in droplet-laden NH_3-O_2 gas with initial droplet density number and diameter of $N_{d,0} = 1.5 \times 10^{12}$ /m^3 and $d_0 = 10$ μm at 115 μs. MS: the location of Mach stem; IW: the location of incident wave; RF: the location of reaction front. Green solid and dashed lines mark IW and RF at $y = 0.002$ m; Orange solid and dashed lines mark MS and RF at $y = -0.002$ m.

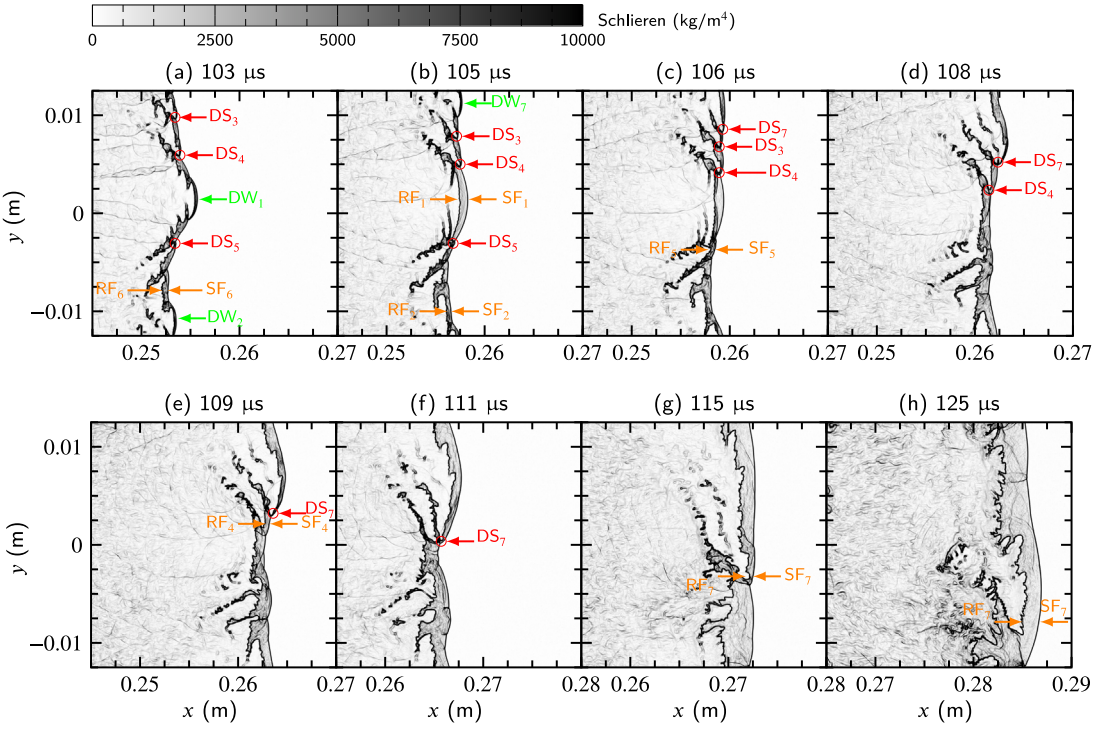

Fig. 11. Evolutions of schlieren fields during detonation extinction in droplet-laden premixed NH_3-O_2 gas with initial droplet density number and diameter of $N_{d,0} = 2.0 \times 10^{12}$ /m^3 and $d_0 = 10$ μm. DW: detonation wave; DS: detonative spot; SF: shock front; RF: reaction front.

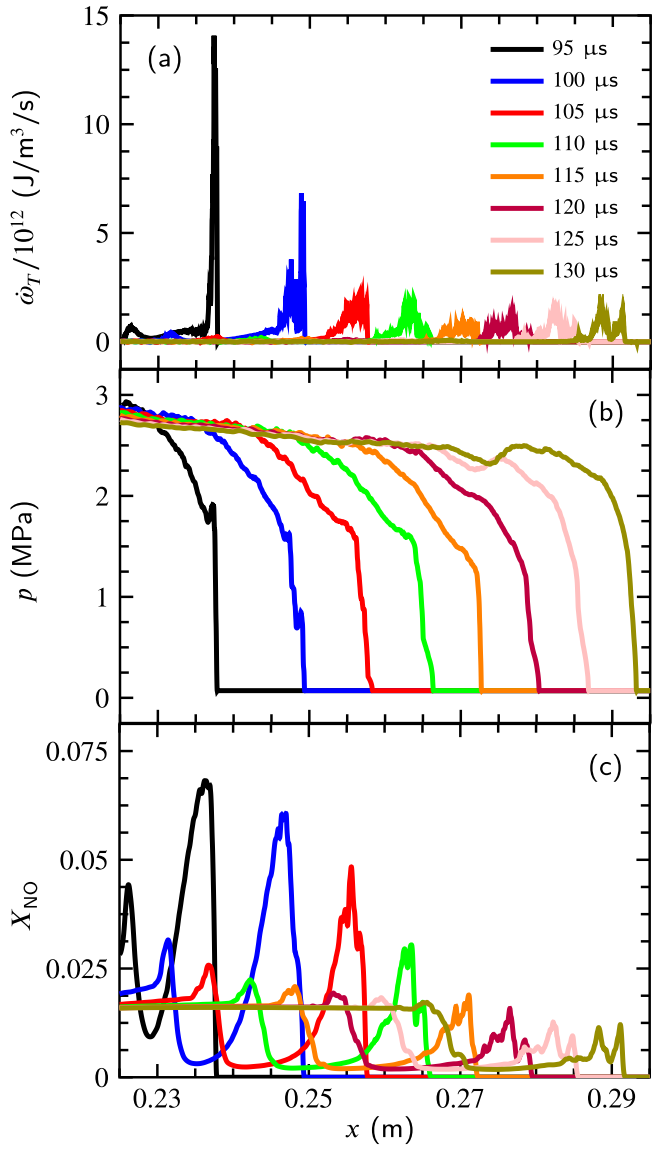

Fig. 12. Spatial profiles of y-direction averaged (a) gaseous heat release rate, $\dot{\omega}_T$, (b) gaseous pressure, p, and (c) gaseous nitric oxide volume fraction, X_{NO}, in droplet-laden NH_3-O_2 gas with initial droplet density number and diameter of $N_{d,0} = 2.0 \times 10^{12}$ /m^3 and $d_0 = 10$ μm.

1330 m/s, respectively. T sharply rises to about 1320 and 1280 K across the MS and the IW, respectively, and then to about 3580 and 3410 K across the corresponding RF. Therefore, the post-MS region experiences higher-intensity detonative combustion and thus droplet evaporative, accelerative, and heating effects than the post-IW region. The values of d are moderately smaller on the whole in the detonated carrier gas behind the MS than the IW. Those of T_d and $u_{d,x}$ are to the contrary.

3.3. Detonation extinction transient

Case C_6 with $N_{d,0} = 2.0{\times}10^{12}$ /m^3 and $d_0 = 10$ μm is selected to analyse the detonation extinction process. Its time sequences of schlieren (density gradient, *i.e.*, $|\nabla\rho|$) fields from 103 to 125 μs are depicted in Fig. 11. Each frame shows a 0.025-m-long section along x-direction of the simulated domain which visualises instantaneous locations of the detonative front. At 103 μs, the DW is locally quenched and highly wrinkled with two bumps, *i.e.*, DW_1 and DW_2, and four depressions, *i.e.*, DS_3-DS_5 and decoupled SF_6-RF_6. DW_1 and DW_2 correspond to Mach stems with coupled SF_1-RF_1 and SF_2-RF_2, respectively. As the ammonia droplets continue to strongly evaporate, accelerate, and absorb heat in the post-DW region, RF_1 and RF_2 see weakened chemical reactivity and reduced propagation speed. They gradually lag behind and decouple with SF_1 and SF_2, respectively, at 105 μs. Simultaneously, DW_7 occurs as DS_3 and DS_4 move downwards. Note that DW_7 is the not-yet decoupled part of DW_2 that leaves and reenters the simulated domain respectively at the bottom and top ends. It experiences partial decoupling and degenerates into DS_7 at the tip of the RF due to the non-uniformity of inter-phase mass, momentum, and energy transfers along y-direction at 106 μs when the SF_5-RF_5 decoupling denotes the quenching of the DW's lower half. DS_7 overtakes DS_3 at 108 μs and decoupled SF_4-RF_4 from DS_4 at 111 μs in succession. It later collides with the SF from the decoupled lower half of the DW and decouples into SF_7 and RF_7 at 115 μs. At 125 μs, the DW ultimately quenches subject to the widened distance between SF_7 and RF_7. In general, the DW degenerates into the DS and then decouples into the SF and RF during the detonation extinction process. Note that Cases C_7–C_9 with the ultimate quenching of DW demonstrate similar extinction transients as Case C_6.

Fig. 12 shows the spatial profiles of y-direction averages of gaseous HRR, $\dot{\omega}_T$, pressure, p, and nitric oxide volume fraction, X_{NO} along x-direction for Case C_6 with $N_{d,0} = 2.0 \times 10^{12}$ /m^3 and $d_0 = 10$ μm. The time interval of 95–130 μs covering the detonation extinction process is addressed. The location of the detonative front is roughly identified where p jumps from the initial pressure of $p_0 = 71$ kPa. The maximum values of $\dot{\omega}_T$, p, and X_{NO} behind the detonative front gradually level off. They roughly decline from 1.4×10^{13} J/m^3/s, 1.9 MPa, and 0.07 at 95 μs to 1×10^{12} J/m^3/s, 1.3 MPa, and 0.02 at 115 μs, respectively, accompanied by the increased exothermic region width with non-zero $\dot{\omega}_T$ due to the elevated wrinkling of the RF, see Figs. 11(a)–(g). The comparatively low $\dot{\omega}_T$, p, and X_{NO} at 115 μs corresponding to the quenched DW, see Figs. 11(g) and (h), are maintained onwards until 130 μs.

4. Conclusions

This work provides an understanding of detonative combustion in two-phase gas-droplet ammonia fuel. The characteristics of detonation propagation and extinction in ammonia droplet-laden premixed NH_3-O_2 gas are numerically investigated in a 2-D planar channel. The present simulations initiate slightly overdriven detonations in the droplet-free carrier gas of which the velocity and cell width demonstrate generally fair accuracy against the corresponding experimental measurements and analytical solutions. The detonation propagation/extinction scenarios with perturbations from the ammonia droplets, parametrised by the initial droplet number density of $N_{d,0} = 1.0 \times 10^{12}$, 1.5×10^{12}, or 2.0×10^{12} /m^3 and diameter of $d_0 = 5$, 10, or 15 μm, are predicted. The major findings are summarised on these points:

(1) The sustained propagation and ultimate quenching of detonation occur under lower and higher values of $N_{d,0}$ and d_0, respectively, and the detonation always quenches under $d_0 = 15$ μm.
(2) The detonation cell structure is considerably changed by the addition of ammonia droplets in the carrier gas and dependent on both d_0 and $N_{d,0}$ along with the detonation propagation/extinction behaviour.
(3) The droplet volume fraction, and the two-phase gas-droplet exchange rates of mass, momentum, and energy exhibit more nonlinear positive correlations with respect to d_0 than $N_{d,0}$.
(4) The ammonia droplets with $d_0 = 5$ and 15 μm under fixed $N_{d,0}$ are completely evaporated, accelerated, and heated most and least quickly, respectively, upon access into the post-detonation wave region.
(5) The droplet-laden detonative combustion and thus droplet evaporative, accelerative, and heating effects in the post-Mach stem region are higher-intensity than the post-incident wave region.

(6) The detonation wave degenerates into detonative spots which then decouple into shock and reaction fronts as quenches, and the gaseous pressure, heat release rate, and nitric oxide volume fraction peaks decline.

CRediT authorship contribution statement

Ruixuan Zhu: Writing – review & editing, Writing – original draft, Visualization, Validation, Software, Methodology, Investigation, Formal analysis, Data curation, Conceptualization. **Guangze Li:** Writing – review & editing, Software, Resources, Methodology, Investigation, Data curation. **Felix Leach:** Writing – review & editing, Resources, Project administration, Funding acquisition. **Martin Davy:** Writing – review & editing, Supervision, Resources, Project administration, Funding acquisition.

Declaration of competing interest

The authors declare that they have no known competing financial interests or personal relationships that could have appeared to influence the work reported in this paper.

Acknowledgements

Ruixuan Zhu gratefully acknowledges the financial support of China Oxford Scholarship Fund and Great Britain China Educational Trust during the completion of this work. Dr. Guangze Li would like to thank the support from the National Natural Science Foundation of China (Grant No. 52306181). The authors acknowledge the use of the University of Oxford Advanced Research Computing (ARC) facility in carrying out this work.

Appendix A. Supplementary data

Supplementary material related to this article can be found online at https://doi.org/10.1016/j.ijhydene.2024.09.432.

References

[1] Valera-Medina A, Xiao H, Owen-Jones M, David W, Bowen P. Ammonia for power. Prog Energy Combust Sci 2018;69:63–102. http://dx.doi.org/10.1016/j.pecs.2018.07.001.

[2] Westlye FR, Ivarsson A, Schramm J. Experimental investigation of nitrogen based emissions from an ammonia fueled SI-engine. Fuel 2013;111:239–47. http://dx.doi.org/10.1016/j.fuel.2013.03.055.

[3] Ryu K, Zacharakis-Jutz GE, Kong S-C. Performance characteristics of compression-ignition engine using high concentration of ammonia mixed with dimethyl ether. Appl Energy 2014;113:488–99. http://dx.doi.org/10.1016/j.apenergy.2013.07.065.

[4] Ezzat M, Dincer I. Energy and exergy analyses of a novel ammonia combined power plant operating with gas turbine and solid oxide fuel cell systems. Energy 2020;194:116750. http://dx.doi.org/10.1016/j.energy.2019.116750.

[5] Okafor EC, Somarathne KKA, Ratthanan R, Hayakawa A, Kudo T, Kurata O, et al. Control of NOx and other emissions in micro gas turbine combustors fuelled with mixtures of methane and ammonia. Combust Flame 2020;211:406–16. http://dx.doi.org/10.1016/j.combustflame.2019.10.012.

[6] Liu Z, Zhou L, Wei H. Experimental investigation on the performance of pure ammonia engine based on reactivity controlled turbulent jet ignition. Fuel 2023;335:127116. http://dx.doi.org/10.1016/j.fuel.2022.127116.

[7] Uddeen K, Tang Q, Shi H, Magnotti G, Turner J. Multiple spark ignition approach to burn ammonia in a spark-ignition engine: An optical study. 2023, SAE Technical Paper, 2023–01–0258.

[8] Mercier A, Mounaïm-Rousselle C, Brequigny P, Bouriot J, Dumand C. Improvement of SI engine combustion with ammonia as fuel: Effect of ammonia dissociation prior to combustion. Fuel Commun 2022;11:100058. http://dx.doi.org/10.1016/j.jfueco.2022.100058.

[9] Huang S-Y, Zhou J, Liu S-J, Peng H-Y, Yuan X-Q. Ammonia/oxygen-enriched air continuous rotating detonation in the hollow chamber. Fuel 2022;311:122166. http://dx.doi.org/10.1016/j.fuel.2021.122166.

[10] Huang S-Y, Zhou J, Liu S-J, Peng H-Y, Yuan X-Q. Continuous rotating detonation engine fueled by ammonia. Energy 2022;252:123911. http://dx.doi.org/10.1016/j.energy.2022.123911.

[11] Akbar R, Kaneshige M, Schultz E, Shepherd J. Detonations in H2-n2o-CH4-NH3-O2-n2 mixtures. In: Explosion dynamics laboratory report FM97-3. Graduate Aeronautical Laboratories, California Institute of Technology; 1997.

[12] Weng Z, Mével R, Chaumeix N. Detonation in ammonia-oxygen and ammonia-nitrous oxide mixtures. Combust Flame 2023;251:112680. http://dx.doi.org/10.1016/j.combustflame.2023.112680.

[13] Ng HD. The effect of chemical reaction kinetics on the structure of gaseous detonations. 2005,

[14] Browne S, Ziegler J, Shepherd J. Numerical solution methods for shock and detonation jump conditions. In: GALCIT report FM2006, vol. 6, Citeseer; 2008, p. 90.

[15] Thomas G. Flame acceleration and the development of detonation in fuel–oxygen mixtures at elevated temperatures and pressures. J Hard Mater 2009;163(2):783–94. http://dx.doi.org/10.1016/j.jhazmat.2008.07.105.

[16] Thomas G, Oakley G, Bambrey R. An experimental study of flame acceleration and deflagration to detonation transition in representative process piping. Process Saf Environ Prot 2010;88(2):75–90. http://dx.doi.org/10.1016/j.psep.2009.11.008.

[17] Li Y, Bi M, Li B, Zhou Y, Huang L, Gao W. Explosion hazard evaluation of renewable hydrogen/ammonia/air fuels. Energy 2018;159:252–63. http://dx.doi.org/10.1016/j.energy.2018.06.174.

[18] Jing Q, Huang J, Liu Q, wang D, Chen X, Wang Z, et al. The flame propagation characteristics and detonation parameters of ammonia/oxygen in a large-scale horizontal tube: As a carbon-free fuel and hydrogen-energy carrier. Int J Hydrog Energy 2021;46(36):19158–70. http://dx.doi.org/10.1016/j.ijhydene.2021.03.032.

[19] Zhu R, Zhao M, Zhang H. Numerical simulation of flame acceleration and deflagration-to-detonation transition in ammonia-hydrogen–oxygen mixtures. Int J Hydrog Energy 2021;46(1):1273–87. http://dx.doi.org/10.1016/j.ijhydene.2020.09.227.

[20] Kohama S, Ito T, Tsuboi N, Ozawa K, Hayashi AK. Two-dimensional detailed numerical simulation of ammonia/hydrogen/air detonation: hydrogen concentration effects and transverse detonation wave structure. Shock Waves 2024;34(2):139–54. http://dx.doi.org/10.1007/s00193-024-01181-6.

[21] Zhu R, Fang X, Xu C, Zhao M, Zhang H, Davy M. Pulsating one-dimensional detonation in ammonia-hydrogen–air mixtures. Int J Hydrog Energy 2022;47(50):21517–36. http://dx.doi.org/10.1016/j.ijhydene.2022.04.265.

[22] Yu Z, Zhang H. End-gas autoignition and knocking combustion of ammonia/hydrogen/air mixtures in a confined reactor. Int J Hydrog Energy 2022;47(13):8585–602. http://dx.doi.org/10.1016/j.ijhydene.2021.12.181.

[23] Xiao H, Valera-Medina A, Bowen PJ. Modeling combustion of ammonia/hydrogen fuel blends under gas turbine conditions. Energy & Fuels 2017;31(8):8631–42.

[24] Roy G, Frolov S, Borisov A, Netzer D. Pulse detonation propulsion: challenges, current status, and future perspective. Prog Energy Combust Sci 2004;30(6):545–672. http://dx.doi.org/10.1016/j.pecs.2004.05.001.

[25] Hishida M, Fujiwara T, Wolanski P. Fundamentals of rotating detonations. Shock Waves 2009;19:1–10.

[26] Sun Z, Huang Y, Luan Z, Gao S, You Y. Three-dimensional simulation of a rotating detonation engine in ammonia/hydrogen mixtures and oxygen-enriched air. Int J Hydrog Energy 2023;48(12):4891–905. http://dx.doi.org/10.1016/j.ijhydene.2022.11.029.

[27] Wang F, Liu Q, Weng C. On the feasibility and performance of the ammonia/hydrogen/air rotating detonation engines. Phys Fluids 2023;35(6):066133. http://dx.doi.org/10.1063/5.0152609.

[28] Kurata O, Iki N, Inoue T, Matsunuma T, Tsujimura T, Furutani H, et al. Development of a wide range-operable, rich-lean low-NOx combustor for NH3 fuel gas-turbine power generation. Proc Combust Inst 2019;37(4):4587–95. http://dx.doi.org/10.1016/j.proci.2018.09.012.

[29] Iki N, Kurata O, Inoue T, Matsunuma T, Tsujimura T, Furutani H, et al. Rich-lean combustor for a 50kw class micro gas turbine firing ammonia. In: Proceeding of global power and propulsion society. 2019, p. 16–8.

[30] Ito S, Uchida M, Fujimori T, Kobayashi H. NOx emission of two-stage combustor for ammonia/natural gas co-fired gas turbine. In: 12th Asia-Pacific conference on combustion. 2019.

[31] Ito S, Uchida M, Kato S, Fujimori T, Kobayashi H. Emission characteristics of a lean-premixed ammonia/natural-gas gas-turbine combustor and effect of secondary ammonia injection. Mech Eng J 2019;6(5):19–00266–19–00266. http://dx.doi.org/10.1299/mej.19-00266.

[32] Verkamp F, Hardin M, Williams J. Ammonia combustion properties and performance in gas-turbine burners. In: Symposium (International) on combustion, vol. 11, (1):1967, p. 985–92. http://dx.doi.org/10.1016/S0082-0784(67)80225-X.

[33] Bull M. Development of an ammonia-burning gas turbine engine. Defense Technical Information Center; 1968.

[34] Scharl V, Lackovic T, Sattelmayer T. Characterization of ammonia spray combustion and mixture formation under high-pressure, direct injection conditions. Fuel 2023;333:126454. http://dx.doi.org/10.1016/j.fuel.2022.126454.

[35] Shen L, Leach F. Effect of ambient pressure on ammonia sprays using a single hole injector. 2024, p. 2024–01–2618, SAE Technical Paper.

[36] Okafor EC, Yamashita H, Hayakawa A, Somarathne KKA, Kudo T, Tsujimura T, et al. Flame stability and emissions characteristics of liquid ammonia spray co-fired with methane in a single stage swirl combustor. Fuel 2021;287:119433. http://dx.doi.org/10.1016/j.fuel.2020.119433.
[37] Okafor EC, Kurata O, Yamashita H, Inoue T, Tsujimura T, Iki N, et al. Liquid ammonia spray combustion in two-stage micro gas turbine combustors at 0.25 MPa; Relevance of combustion enhancement to flame stability and NOx control. Appl Energy Combust Sci 2021;7:100038. http://dx.doi.org/10.1016/j.jaecs.2021.100038.
[38] Zhang Z, Long W, Cui Z, Dong P, Tian J, Tian H, et al. Visualization study on the ignition and diffusion combustion process of liquid phase ammonia spray ignited by diesel jet in a constant volume vessel. Energy Convers Manage 2024;299:117889. http://dx.doi.org/10.1016/j.enconman.2023.117889.
[39] Somarathne K, Yamashita H, Colson S, Okafor E, Hayakawa A, Kudo T, et al. Liquid ammonia spray combustion and emission characteristics with gaseous hydrogen/air co-firing. In: Proceedings of the 13th Asia-Pacific conference on combustion. 2021.
[40] Somarathne KDKA, Yamashita H, Colson S, Oku K, Honda K, Okafor EC, et al. Towards the development of liquid ammonia/air spray combustion in a gas turbine-like combustor at moderately high pressure. Appl Energy Combust Sci 2023;16:100215. http://dx.doi.org/10.1016/j.jaecs.2023.100215.
[41] Lewandowski MT, Pasternak M, Haugsvær M, Løvås T. Simulations of ammonia spray evaporation, cooling, mixture formation and combustion in a direct injection compression ignition engine. Int J Hydrog Energy 2024;52:916–35. http://dx.doi.org/10.1016/j.ijhydene.2023.06.143.
[42] Zhu R, Huang Z, Xu C, Wu B, Davy M. Integration and validation of some modules for modelling of high-speed chemically reactive flows in two-phase gas-droplet mixtures. Comput & Fluids 2024;277:106282. http://dx.doi.org/10.1016/j.compfluid.2024.106282.
[43] Zhu R, Huang Z, Xu C, Fang X, Zhang H, Davy M. Large eddy simulation of a supersonic lifted hydrogen flame: Impacts of Lewis, turbulent Schmidt and Prandtl numbers. Phys Fluids 2024;36(7):075118. http://dx.doi.org/10.1063/5.0214630.
[44] Weller HG, Tabor G, Jasak H, Fureby C. A tensorial approach to computational continuum mechanics using object-oriented techniques. Comput Phys 1998;12(6):620–31. http://dx.doi.org/10.1063/1.168744.
[45] Mével R, Javoy S, Lafosse F, Chaumeix N, Dupré G, Paillard C-E. Hydrogen–nitrous oxide delay times: Shock tube experimental study and kinetic modelling. Proc Combust Inst 2009;32(1):359–66. http://dx.doi.org/10.1016/j.proci.2008.06.171.
[46] Greenshields CJ, Weller HG, Gasparini L, Reese JM. Implementation of semi-discrete, non-staggered central schemes in a colocated, polyhedral, finite volume framework, for high-speed viscous flows. Internat J Numer Methods Fluids 2010;63(1):1–21. http://dx.doi.org/10.1002/fld.2069.
[47] Kee RJ, Rupley FM, Meeks E, Miller JA. CHEMKIN-III: A FORTRAN chemical kinetics package for the analysis of gas-phase chemical and plasma kinetics. Sandia National Lab; 1996, SAND–96–8216.
[48] Yao MX, Hickey J-P, Ma PC, Ihme M. Molecular diffusion and phase stability in high-pressure combustion. Combust Flame 2019;210:302–14. http://dx.doi.org/10.1016/j.combustflame.2019.08.036.
[49] Bruno C, Sankaran V, Kolla H, Chen JH. Impact of multi-component diffusion in turbulent combustion using direct numerical simulations. Combust Flame 2015;162(11):4313–30. http://dx.doi.org/10.1016/j.combustflame.2015.07.013.
[50] Hasadi YMFE, Padding JT. On the existence of logarithmic terms in the drag coefficient and nusselt number of a single sphere at high Reynolds numbers. 2020, arXiv: Fluid Dynamics.
[51] Whitaker S. Forced convection heat transfer correlations for flow in pipes, past flat plates, single cylinders, single spheres, and for flow in packed beds and tube bundles. AIChE J 1972;18(2):361–71. http://dx.doi.org/10.1002/aic.690180219.
[52] Xu C, Gao Y, Ren Z, Lu T. A sparse stiff chemistry solver based on dynamic adaptive integration for efficient combustion simulations. Combust Flame 2016;172:183–93. http://dx.doi.org/10.1016/j.combustflame.2016.07.009.
[53] Wu B, Zhao X, Chowdhury BR, Cetegen BM, Xu C, Lu T. A numerical investigation of the flame structure and blowoff characteristics of a bluff-body stabilized turbulent premixed flame. Combust Flame 2019;202:376–93. http://dx.doi.org/10.1016/j.combustflame.2019.01.026.
[54] Gao Y, Liu Y, Ren Z, Lu T. A dynamic adaptive method for hybrid integration of stiff chemistry. Combust Flame 2015;162(2):287–95. http://dx.doi.org/10.1016/j.combustflame.2014.07.023.
[55] Schwer DA, Tolsma JE, Green WH, Barton PI. On upgrading the numerics in combustion chemistry codes. Combust Flame 2002;128(3):270–91. http://dx.doi.org/10.1016/S0010-2180(01)00352-2.
[56] Crank J, Nicolson P. A practical method for numerical evaluation of solutions of partial differential equations of the heat-conduction type. Math Proc Cambridge Philos Soc 1947;43(1):50–67. http://dx.doi.org/10.1017/S0305004100023197.
[57] Kurganov A, Noelle S, Petrova G. Semidiscrete central-upwind schemes for hyperbolic conservation laws and Hamilton–Jacobi equations. SIAM J Sci Comput 2001;23(3):707–40. http://dx.doi.org/10.1137/S1064827500373413.
[58] van Leer B. Towards the ultimate conservative difference scheme. II. Monotonicity and conservation combined in a second-order scheme. J Comput Phys 1974;14(4):361–70. http://dx.doi.org/10.1016/0021-9991(74)90019-9.
[59] Macpherson GB, Nordin N, Weller HG. Particle tracking in unstructured, arbitrary polyhedral meshes for use in CFD and molecular dynamics. Commun Numer Methods Eng 2009;25(3):263–73. http://dx.doi.org/10.1002/cnm.1128.
[60] Dukowicz JK. A particle-fluid numerical model for liquid sprays. J Comput Phys 1980;35(2):229–53. http://dx.doi.org/10.1016/0021-9991(80)90087-X.
[61] Abramzon B, Sirignano W. Droplet vaporization model for spray combustion calculations. Int J Heat Mass Transfer 1989;32(9):1605–18. http://dx.doi.org/10.1016/0017-9310(89)90043-4.
[62] Liu AB, Mather D, Reitz RD. Modeling the effects of drop drag and breakup on fuel sprays. 1993, 970032, SAE Technical Paper.
[63] Crowe CT, Schwarzkopf JD, Sommerfeld M, Tsuji Y. Multiphase flows with droplets and particles. CRC Press; 2011.
[64] Gutiérrez Marcantoni L, Tamagno J, Elaskar S. RhoCentralRfFoam: An OpenFOAM solver for high speed chemically active flows – Simulation of planar detonations –. Comput Phys Comm 2017;219:209–22. http://dx.doi.org/10.1016/j.cpc.2017.05.021.
[65] Huang Z, Zhao M, Xu Y, Li G, Zhang H. Eulerian-Lagrangian modelling of detonative combustion in two-phase gas-droplet mixtures with OpenFOAM: Validations and verifications. Fuel 2021;286:119402. http://dx.doi.org/10.1016/j.fuel.2020.119402.
[66] Gutiérrez Marcantoni L, Tamagno J, Elaskar S. A numerical study on the impact of chemical modeling on simulating methane-air detonations. Fuel 2019;240:289–98. http://dx.doi.org/10.1016/j.fuel.2018.11.147.
[67] Gutiérrez Marcantoni L, Tamagno J, Elaskar S. Two-dimensional numerical simulations of detonation cellular structures in H2-O2-Ar mixtures with OpenFOAM®. Int J Hydrog Energy 2017;42(41):26102–13. http://dx.doi.org/10.1016/j.ijhydene.2017.08.188.
[68] Zhao M, Li J-M, Teo CJ, Khoo BC, Zhang H. Effects of variable total pressures on instability and extinction of rotating detonation combustion. Flow Turbul Combust 2020;104:261–90. http://dx.doi.org/10.1007/s10494-019-00050-y.
[69] Zhao M, Zhang H. Origin and chaotic propagation of multiple rotating detonation waves in hydrogen/air mixtures. Fuel 2020;275:117986. http://dx.doi.org/10.1016/j.fuel.2020.117986.
[70] Zhao M, Cleary MJ, Zhang H. Combustion mode and wave multiplicity in rotating detonative combustion with separate reactant injection. Combust Flame 2021;225:291–304. http://dx.doi.org/10.1016/j.combustflame.2020.11.001.
[71] Zhao M, Zhang H. Rotating detonative combustion in partially pre-vaporized dilute n-heptane sprays: Droplet size and equivalence ratio effects. Fuel 2021;304:121481. http://dx.doi.org/10.1016/j.fuel.2021.121481.
[72] Xu Y, Zhang H. Interactions between a propagating detonation wave and circular water cloud in hydrogen/air mixture. Combust Flame 2022;245:112369. http://dx.doi.org/10.1016/j.combustflame.2022.112369.
[73] Xu Y, Zhang H. Pulsating propagation and extinction of hydrogen detonations in ultrafine water sprays. Combust Flame 2022;241:112086. http://dx.doi.org/10.1016/j.combustflame.2022.112086.
[74] Huang Z, Xu Y, Li S, Meng Q, Zhang H. Detailed simulations of one-dimensional detonation propagation in dilute n-heptane spray and air mixtures. Phys Fluids 2023;35(12):126116. http://dx.doi.org/10.1063/5.0173991.
[75] Meng Q, Zhao M, Xu Y, Zhang L, Zhang H. Structure and dynamics of spray detonation in n-heptane droplet/vapor/air mixtures. Combust Flame 2023;249:112603. http://dx.doi.org/10.1016/j.combustflame.2022.112603.
[76] Xu Y, Zhao M, Zhang H. Extinction of incident hydrogen/air detonation in fine water sprays. Phys Fluids 2021;33(11):116109. http://dx.doi.org/10.1063/5.0071405.
[77] Xu Y, Zhang P, Meng Q, Li S, Zhang H. Transmission of hydrogen detonation across a curtain of dilute inert particles. Combust Flame 2023;254:112834. http://dx.doi.org/10.1016/j.combustflame.2023.112834.
[78] Lee JHS. The detonation phenomenon. Cambridge University Press; 2008.
[79] Watanabe H, Matsuo A, Chinnayya A, Matsuoka K, Kawasaki A, Kasahara J. Numerical analysis of the mean structure of gaseous detonation with dilute water spray. J Fluid Mech 2020;887:A4. http://dx.doi.org/10.1017/jfm.2019.1018.
[80] Weng Z, Mével R. Implementation of an OpenFOAM solver for shock and detonation simulation at high pressure. Comput & Fluids 2023;265:106012. http://dx.doi.org/10.1016/j.compfluid.2023.106012.
[81] Raman V, Prakash S, Gamba M. Nonidealities in rotating detonation engines. Annu Rev Fluid Mech 2023;55(1):639–74. http://dx.doi.org/10.1146/annurev-fluid-120720-032612.
[82] Xiao H, Oran ES. Shock focusing and detonation initiation at a flame front. Combust Flame 2019;203:397–406. http://dx.doi.org/10.1016/j.combustflame.2019.02.012.
[83] Zhu R, Tang S, Lai S, Fang X, Davy M, Xu C. Parametric Studies of Deflagration-to-Detonation Transition in a Pre-Chamber/Main-Chamber System. In: Internal combustion engine division fall technical conference, ASME 2022 ICE forward conference. 2022, V001T06A003.
[84] Huang Z, Zhang H. On the interactions between a propagating shock wave and evaporating water droplets. Phys Fluids 2020;32(12):123315. http://dx.doi.org/10.1063/5.0035968.